Santos, J. T.; Li, Jian; Ilves, J.; Ockeloen-Korppi, C. F.; Sillanpaa, M.

Optomechanical measurement of a millimeter-sized mechanical oscillator approaching the quantum ground state

Published in:
New Journal of Physics

DOI:
10.1088/1367-2630/aa83a5

Published: 12/10/2017

Document Version
Publisher's PDF, also known as Version of record

PAPER • OPEN ACCESS

Optomechanical measurement of a millimeter-sized mechanical oscillator approaching the quantum ground state

To cite this article: J T Santos *et al* 2017 *New J. Phys.* **19** 103014

New Journal of Physics
The open access journal at the forefront of physics

Deutsche Physikalische Gesellschaft DPG
IOP Institute of Physics

Published in partnership with: Deutsche Physikalische Gesellschaft and the Institute of Physics

OPEN ACCESS

RECEIVED
10 March 2017

REVISED
27 July 2017

ACCEPTED FOR PUBLICATION
2 August 2017

PUBLISHED
12 October 2017

PAPER

Optomechanical measurement of a millimeter-sized mechanical oscillator approaching the quantum ground state

J T Santos[1], J Li[2,3], J Ilves[1], C F Ockeloen-Korppi[1] and M Sillanpää[1,4]

[1] Department of Applied Physics, Aalto University, PO Box 15100, FI-00076 AALTO, Finland
[2] School of Engineering, University of Glasgow, Glasgow, G12 8LT, United Kingdom
[3] Interdisciplinary Center of Quantum Information, College of Science, National University of Defense Technology, Changsha 410073, People's Republic of China
[4] Author to whom any correspondence should be addressed.

E-mail: mika.sillanpaa@aalto.fi

Keywords: optomechanics, superconducting qubits, mechanical oscillators

Abstract

Cavity optomechanics is a tool to study the interaction between light and micromechanical motion. Here we observe optomechanical physics in a truly macroscopic oscillator close to the quantum ground state. As the mechanical system, we use a mm-sized piezoelectric quartz disk oscillator. Its motion is coupled to a charge qubit which translates the piezo-induced charge into an effective radiation–pressure interaction between the disk and a microwave cavity. We measure the thermal motion of the lowest mechanical shear mode at 7 MHz down to 30 mK, corresponding to roughly 10^2 quanta in a 20 mg oscillator. We estimate that with realistic parameters, it is possible to utilize the back-action cooling by the qubit in order to control macroscopic motion by a single Cooper pair. The work opens up opportunities for macroscopic quantum experiments.

1. Introduction

Small but nevertheless macroscopic systems have been operated in the limit where they exhibit quantum mechanical behavior in some of their degrees of freedom. One of the most successful systems have been the superconducting quantum bits (qubits) [1, 2], where the most complicated quantum states have been constructed [3, 4]. Observing mechanical oscillators at the quantum limit of their motion, where the excess phonon number $n_{\rm m}$ approaches zero, was a long-standing goal. The ground state was reached some years ago [5–7]. In earlier experiments, $n_{\rm m} < 10^2$ was reached with nanostrings already a decade ago [8–10]. In the cavity optomechanical scheme, where optical and mechanical resonances are coupled [11], micro mirrors up to 0.2 mg weight [12–14], cantilevers [15–17] up to 0.5 mm long, or nitride membranes [18] have been used. Ground-state cooling [6], entanglement [19], and squeezed mechanical states [20–22] have been reported in the realization involving superconducting radio frequency cavities together with drum oscillators. A major motivation is to study the fundamentals of quantum mechanics.

Here we propose and demonstrate a new cavity optomechanical scheme which involves a genuinely macroscopic mechanical oscillator relatively near the ground state (see figure 1). We use a 6 mm diameter quartz disk oscillator with a total mass of 20 mg, and the vibrating effective mass of the order 0.1 mg, whose vibrations at the lowest shear mode frequency $\omega_{\rm m}/2\pi \simeq 7$ MHz we observe at a temperature of 30 mK. The quartz disk is used both as the mechanical oscillator, and as a substrate for fabricating a superconducting micro circuit. The latter includes a charge qubit and a transmission line resonator. With the notable exception of LIGO [23], it is among the most macroscopic system in such studies. Our system is three orders of magnitude more massive than earlier [24], and in terms of mass over measured phonon number, it is two decades more macroscopically quantum.

The work is based on a generic idea where a quantum two-level system, a qubit, mediates and enhances an interaction between a linear mechanical oscillator and a linear cavity. For example, the energy of a charge qubit depends sensitively on the charge in its vicinity, and the frequency of an electrical system consisting of the qubit

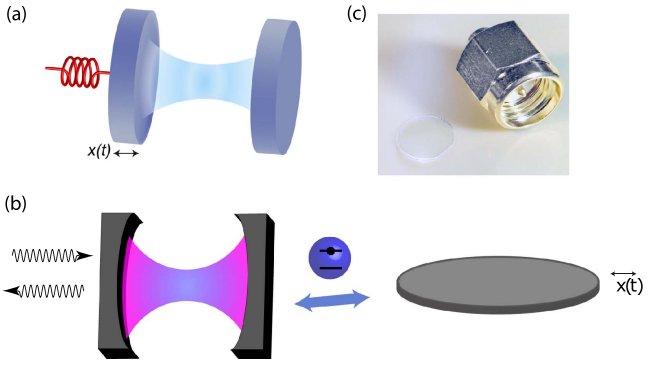

Figure 1. Piezo optomechanics. (a) Illustration of a prototype cavity optomechanical system. (b) In the current work, a quantum two-level system (qubit) mediates an optomechanical interaction between a macroscopic quartz oscillator and an electromagnetic cavity. (c) Photograph of the quartz chip used in the experiment, beside an SMA connector.

and a cavity coupled to the qubit becomes charge-sensitive. A voltage-biased conductive mechanical oscillator was proposed to this end in [25, 26], and the scheme was experimentally demonstrated in [27]. An analogous setup has been proposed using a flux-biased qubit [28]. The main motivation for introducing a qubit is that the qubit can dramatically enhance the effective optomechanical interaction, possibly allowing for entering the elusive single-photon strong coupling regime.

In the current work, the charge sensed by a charge qubit arises due to the piezoelectricity of the quartz oscillator. The deformation corresponding to the mechanical vibrations induces charge on the chip surface. Here, the role of the qubit is particularly critical. The piezo oscillations and the on-chip microwave cavity as such do couple to each other, however, that is a small linear coupling of two linear, highly detuned oscillators. That coupling as such is of very limited use. In a recent theory proposal [29], a related system was introduced where a coupling between a transmon qubit and piezo vibrations was mediated via a low-frequency cavity, but the optomechanical aspect was not considered.

2. The optomechanical system

2.1. Radiation–pressure interaction

As illustrated in figure 1(a), the traditional cavity optomechanics setup involves two optical mirrors facing each other, assembled such that one of the mirrors is free to oscillate. The cavity and the mechanical oscillator have the resonance frequencies ω_c and $\omega_m \ll \omega_c$, and decay rates κ and $\gamma \ll \kappa$, respectively. The coupled system is described by the radiation–pressure Hamiltonian, which couples the cavity and the mechanical oscillator, and reads

$$H = \omega_c a^\dagger a + \omega_m b^\dagger b + g_0 a^\dagger a (b^\dagger + b). \tag{1}$$

Here, $a^\dagger$ and $b^\dagger$ are the creation operators of the cavity and the mechanical oscillator, respectively. The single-quantum coupling energy $g_0 \ll \kappa$ is the small parameter in the system. Experimentally, it is often the most important figure in the sense that it sets limits for how strong mechanics–cavity interaction one can obtain. One usually strongly pumps the cavity up to a photon number $n_P \gg 1$. As a result, the relevant coupling is the effective coupling $G = g_0\sqrt{n_P}$.

The significance of the cavity interaction on the mechanical oscillator dynamics is described by the cooperativity $C = \frac{4G^2}{\kappa\gamma}$, or alternatively by a decoherence parameter $\eta = \frac{C}{n_m^T}$. Here, $n_m^T \simeq k_B T/(\hbar\omega_m)$ is the equilibrium phonon number set by coupling to a bath of temperature T. The η quantity describes what is the importance of the cavity back-action on the oscillator decoherence due to the bath, and it is often the single most relevant parameter in the quantum experiments. The basic optomechanical phenomenon is the dynamic back-action from the cavity. It appears as an optically induced change in damping to $\gamma_{eff} = \gamma \pm \gamma_{opt}$, with $\gamma_{opt} = 4G^2/\kappa$, leading either to sideband cooling or lasing. The effective phonon number becomes $n_m = n_m^T \gamma/\gamma_{eff}$.

2.2. Qubit-mediated optomechanics

As already mentioned, systems described by equation (1) can be physically built from very different ingredients. In qubit-mediated cavity optomechanics [25–28, 34], see figure 1(b), the qubit can drastically enhance the intrinsically small radiation–pressure coupling g_0 between the mechanics and an microwave cavity. This is

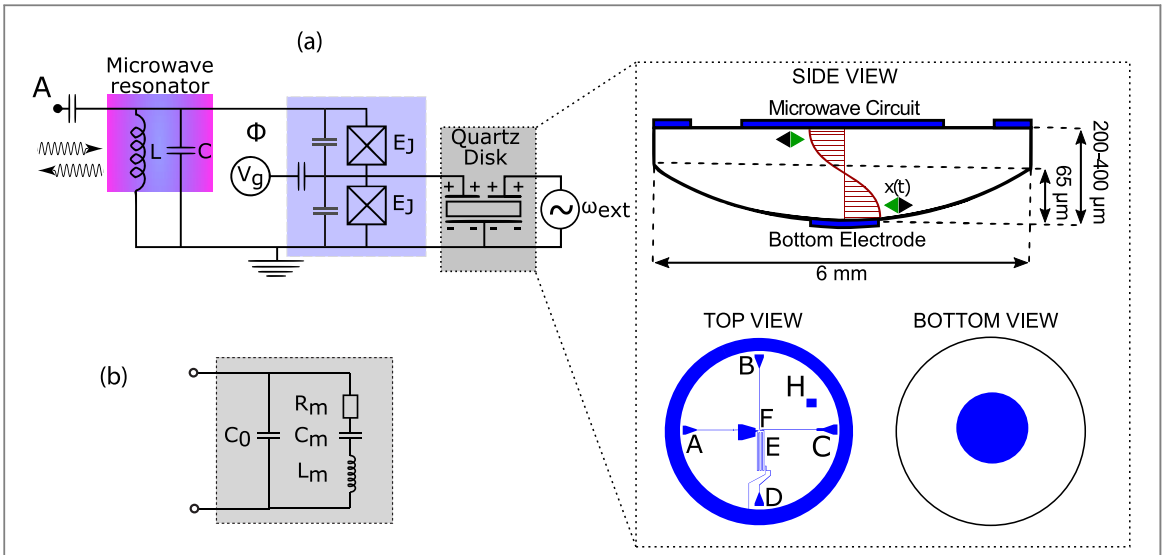

Figure 2. Device schematics. (a) Representation of the quartz disk oscillator, qubit, and microwave resonator. The charge qubit is contained within the blue box. The circuit is fabricated directly on top of the flat surface of a quartz disk with plano-convex profile, which traps the mechanical energy in the middle, thereby increasing mechanical Q-values [30–33]. The lowest shear mode at 7 MHz couples to the microwave circuit. Blue denotes aluminum metallization, and white is bare quartz. The bonding pads are labeled as: A is the input/output for the reflection measurement, B is the gate bias, C is a test junction, D is the flux bias, E is the on-chip inductor L, F is the junctions and island region, and H is used for actuating the mechanical vibrations in order to test the system before the actual experiments. (b) Equivalent electrical resonator of the piezoelectric quartz oscillator.

because a large linear coupling, created by applying a dc bias to the qubit, becomes converted into an effective parametric coupling as reviewed in the following.

The charge qubit, considered in this work, consists of two small-area Josephson junctions defining an island as shown in figure 2(a). The junctions are supposed to have equal Josephson energies E_J. The junctions, island, and a capacitive gate contribute to the sum capacitance C_Σ of the qubit, which provides the charging energy of a single electron as $E_C = e^2/2C_\Sigma$. The charge qubit limit, $E_J/E_C \lesssim 1$, entails a strong dependence of the qubit energy on the charge q_g polarized on the qubit island. In the following, we use a dimensionless charge $n_g = q_g/2e$ in units of the Cooper-pair charge $2e$. Besides the gate charge, the qubit energy can be controlled by a magnetic flux Φ in the superconducting loop shown in figure 2(a). The Hamiltonian of the qubit is $H_q = -\frac{B_x}{2}\sigma_x - \frac{B_z}{2}\sigma_z$. The effective magnetic fields are $B_x = 2E_J\cos(\pi\Phi/\Phi_0)$, $B_z = 4E_C(1-2n_g)$, and σ_x and σ_z are the Pauli spin matrices. The coupling of the charge qubit to mechanical oscillators is described by $H_{qm} = g_m i\sigma_z(b^\dagger - b)$, where g_m is the coupling energy. In the case of capacitive coupling to vibrating metallic beams or membranes [35, 36], g_m is proportional to a dc voltage bias, and can be a sizable fraction of the oscillator frequency.

In order to create the optomechanical interaction starting from the qubit–oscillator coupling, we include in the circuit design a transmission line resonator, which shunts the qubit, as presented in figure 2(a). We label the qubit–cavity coupling energy as g_{qc}. The radiation–pressure interaction can be derived by considering the microwave cavity having the Hamiltonian $H = \omega_c a^\dagger a$. The cavity frequency ω_c is Lamb shifted from the intrinsic value ω_{c0} as $\omega_c \simeq \omega_{c0} + g_{qc}^2/\Delta$, where Δ is the detuning between qubit and cavity frequencies. Supposing the qubit stays in the ground state, the detuning becomes $\Delta \Rightarrow \Delta - 2ig_m(b^\dagger - b)$. The cavity Hamiltonian now assumes the form $H = g_0 a^\dagger a(b^\dagger + b)$, where the (single photon) radiation–pressure coupling is $g_0 = 2(g_{qc}/\Delta)^2 g_m$.

2.3. Coupling to piezo motion

Let us return to description of the piezo oscillator. We consider a piezoelectric disk having thickness t, shear mode stress coefficient e_s of the material, shear modulus Y_s, and relative permittivity ϵ_r. One further defines the dimensionless piezoelectric coupling coefficient $K_0^2 = e_s^2/(\epsilon_r\epsilon_0 Y_s)$. A shear deformation by a characteristic distance x corresponds to a shear strain $\lambda_s = x/t$, and generates a piezoelectric surface charge density $\sigma_q = \lambda_s e_s$. A piezoelectric oscillator is made by metallizing both surfaces of the chip over an area A. The geometric capacitance in the plate-capacitor approximation is then $C_0 = \epsilon_r\epsilon_0 A/t$. The oscillator can be represented as an equivalent series LCR resonator (figure 2(b)) with the effective parameters $C_m = K_0^2 C_0$, $L_m = [(2\pi\omega_m)^2 C_m]^{-1}$ and $R_m = (\omega_m C_m Q)^{-1}$, with Q the mechanical quality factor. The corresponding quantized harmonic oscillator exhibits zero-point vibrations of an amplitude $x_{zp} = \sqrt{\hbar/2M\omega_m}$, where M is the effective mass. In case of our macroscopic oscillator, x_{zp} is very small, in the range of 10^{-18}–10^{-19} m. Using the

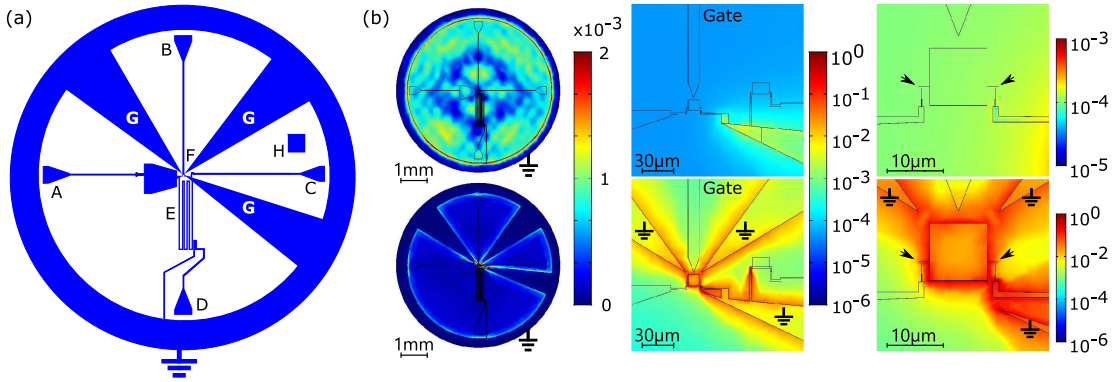

Figure 3. Focusing of the piezo charge. (a) Circuit layout engaging three grounded spikes (labeled G). Other labels are as in figure 2(b). Blue denotes aluminum metallization, and white is bare quartz. (b) Simulation of the piezoelectric surface charge density induced by the lowest mechanical shear mode vibrations of the quartz disk. The top row shows the results for the layout in figure 2(a), while the bottom row displays the behavior of a charge focusing layout shown in (a). The values are scaled by the maximum in the focusing layout. The qubit junctions are marked by arrows.

equivalent circuit (see appendix A), the qubit–piezo interaction can be derived as $g_{\rm m} = \frac{2E_{\rm C}}{e}\sqrt{\frac{C_{\rm m}\hbar\omega_{\rm m}}{2}}$. The effective radiation–pressure interaction between the piezo motion and a cavity frequency arises then as discussed in section 2.2. Notice that in contrast to previous work where the qubit acts as to enhance the radiation–pressure interaction, in the present case the qubit is needed in order to get any coupling whatsoever.

3. Optimizing device parameters

Next we will work out some numbers using the parameters of the experiment discussed below. We begin with the interaction of the qubit and cavity. Typically [25, 27], $g_{\rm qc}/\omega_{\rm c} \approx 0.1$, thus the qubit and cavity are close to the ultra-strong coupling regime [37]. The analysis presented in the end of section 2.2 holds only if $\Delta \gg g_{\rm qc}$, so it is not immediately clear how large a ratio $g_0/g_{\rm m}$ one can achieve. In order to make quantitative estimates of the radiation–pressure coupling, we treat the effective cavity as a charge-tunable resonator. The radiation–pressure coupling is $g_0 \equiv \frac{\partial\omega_{\rm c}}{\partial x}x_{\rm zp} = \frac{\partial\omega_{\rm c}}{\partial n_{\rm g}}n^0_{\rm zp}$, where we define the number of charges in the surface area under the qubit island corresponding to zero-point motion, $n^0_{\rm zp} = \frac{\partial n_{\rm g}}{\partial x}x_{\rm zp}$. In terms of the piezo-induced charge density $\sigma_{\rm q}$, the number of charges in the surface area under the qubit island with area $A_{\rm qb}$ is $n^0_{\rm zp} = \sigma_{\rm q}A_{\rm qb}$.

For the moment we suppose the piezo charge density is uniformly spread across the quartz disk surface, thus $n^0_{\rm zp} = \frac{x_{\rm zp}e_{\rm s}A_{\rm qb}}{2et}$. Quartz has the material parameters $e_{\rm s} \approx 0.1$ C m^{-2}, $K_0^2 \approx 0.01$, $Y_{\rm s} \approx 30$ GPa and $\epsilon_{\rm r} \approx 4.0$. We use circular disks with surface area $A \approx \pi \cdot (3\ {\rm mm})^2$ and thickness $t \approx 400\ \mu$m. Given a typical qubit island $A_{\rm qb} \approx (10\ \mu{\rm m})^2$, we obtain $n^0_{\rm zp} \approx 10^{-8}$, which is very small compared to typical charge sensitivities in microwave single-electron devices, in the range of 10^{-6} to 10^{-4} Hz$^{-1/2}$. With a good choice of parameters of the qubit and the microwave cavity [27], the modulation of cavity frequency as a function of charge is of the order $\frac{\partial\omega_{\rm c}}{\partial n_{\rm g}} \approx (2\pi) \cdot 50$ MHz, and we estimate $g_0 \approx 2\pi \cdot 1$ Hz. This is two orders of magnitude smaller than typical of aluminum drum oscillators [6], and is mostly limited by the small island $A_{\rm qb}/A \ll 1$.

Instead of enlarging the qubit island in order to increase $g_0 \propto n^0_{\rm zp} = \sigma_{\rm q}A_{\rm qb}$, our primary strategy is to focus most of the piezo charge nearby the island. This is achieved through manipulation of the mechanical mode shape, thereby locally increasing $\sigma_{\rm q}$. We use Comsol Multiphysics simulations with an actuation electrode to drive the mode, and adjust the drive such that the strain energy equals the mode zero-point energy. Then we integrate the piezo charge around the island to obtain $n^0_{\rm zp}$.

The basic circuit layout used in earlier related work [27] is shown in figure 2(a), and the corresponding normalized charge density in the top row of figure 3(b), where we observe an approximately uniform density all over the chip. For the final design shown in figure 3(a), we add grounded spikes which extend from the ground planes surrounding the chip towards the qubit island. The spikes strongly enhance the nearby electric field and act as anchors, focusing most of the piezoelectric strain/charge to the center of the disk (bottom row of figure 3(b)). Comparing the realizations in figure 3(b), the integrated charge around the qubit island differs by two orders of magnitude in favor of the charge focusing design, translating into a dramatic increase in the radiation–pressure coupling.

Table 1. Parameters and simulation results of the devices 1 and 2 measured in this work, and for a hypothetical device 3.

Device	Island size	C_0	n_{zp}^0 (no focusing)	n_{zp}^0 (focusing)	Focusing ratio	$g_0/2\pi$ ($\Phi = \Phi_0/2$, $n_g = 0.4$)	E_J/E_C
1	$(10\ \mu m)^2$	0.7 fF	3×10^{-8}	2×10^{-6}	70	90 Hz	0.45
2	$(20\ \mu m)^2$	2.2 fF	1×10^{-7}	7×10^{-6}	70	530 Hz	0.73
3	$(380\ \mu m)^2$	42 fF	1×10^{-7}	2×10^{-4}	6	18 kHz	5.4

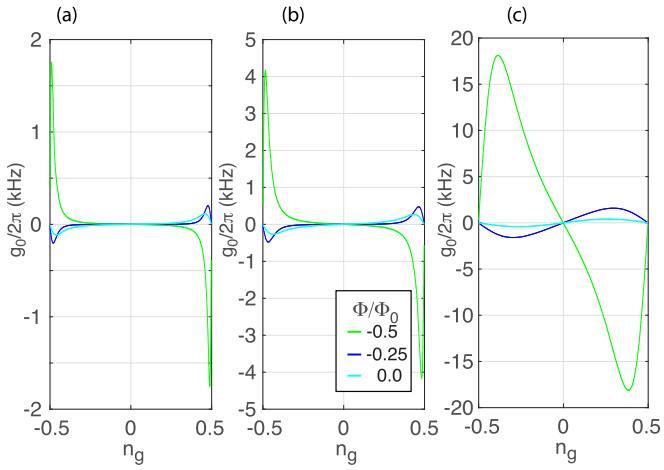

Figure 4. Predicted single-photon coupling g_0 as a function of gate charge and flux bias. Parameter values are as in the current experiment. (a) Device 1 (island size $(10\ \mu m)^2$). (b) Device 2 (island size $(20\ \mu m)^2$). (c) Optimized device 3 (island size $(380\ \mu m)^2$).

The other property contributing to the coupling is the charge dispersion $\frac{\partial \omega_c}{\partial n_g}$ which we obtain by numerically diagonalizing the charge qubit Hamiltonian. This quantity depends on both the qubit and cavity properties and on the gate and flux bias, and it is sensitive to the E_J/E_C ratio, strongly enhanced in the deep charge qubit limit $E_J/E_C \ll 1$, suggesting that g_0 is maximized in the said limit. Nonetheless, as explained below, nearly the opposite holds true.

In the simulations we consider three potentially realizable devices which substantially differ in the island size as written in the second column of table 1. In figure 4 we plot the predicted coupling for the three devices as a function of gate charge. A device with a small island and consequently small capacitance (figure 4(a)), benefits from large maximum values $\partial\omega_c/\partial n_g$ that causes the predicted g_0 to strongly peak near $n_g = \pm 0.5$ as seen in figure 4(a). By increasing the island size (figure 4(b)), the charge modulation is decreased, but this is overwhelmed by a substantially larger integrated charge. At small island size, g_0 grows roughly proportional to the island size. Before reaching a very large island as in device 3 (figure 4(c)), the dependence levels off, on one hand because charge focusing loses its effect at large size, on the other hand because charge dispersion is reduced. Device 3 represents a design which is expected to roughly maximize the radiation–pressure coupling. Notice that the island can be made much larger than that of a typical charge sensitive device, owing to the low dielectric constant $\epsilon_r \approx 4$ of quartz which keeps the capacitance moderate.

As seen in figure 4, in the optimum bias points, g_0 can attain values up to several kHz. These values are an order of magnitude higher than those of mesoscopic aluminum drum oscillators, showing a great promise for the proposed scheme. We note that in spite that large values are predicted in the charge qubit limit (figures 4(a) and (b)), these values may not be reachable in practice. Namely, large $\frac{\partial \omega_c}{\partial n_g}$ implies a high sensitivity to background charge fluctuations. This entails a strong dephasing of the effective cavity, visible as an inhomogeneously broadened resonance, or a fast cavity decay. The latter have been prohibiting reaching the single–photon strong coupling limit in [27], and as we see later in section 4, these effects are present in the current experiment as well.

We now briefly discuss the effective mass related to the quartz vibrations. In the case that the shear mode is spread all over the disk as roughly in figure 3(b) (top), the effective mass of the mode is the disk mass times a geometric factor of the order but smaller than one. Since charge focusing also focuses mechanical strain in the same ratio as charge is focused, also the vibrating effective mass is clearly reduced as a result. A rough estimate is that the effective mass is of the order the disk mass divided by the focusing ratio, in the present experiment we obtain ~0.1 mg. We note, finally, that in spite of the focusing, non-negligible part of the vibrations are delocalized all over the 6 mm chip, hence substantiating the claims of true macroscopity.

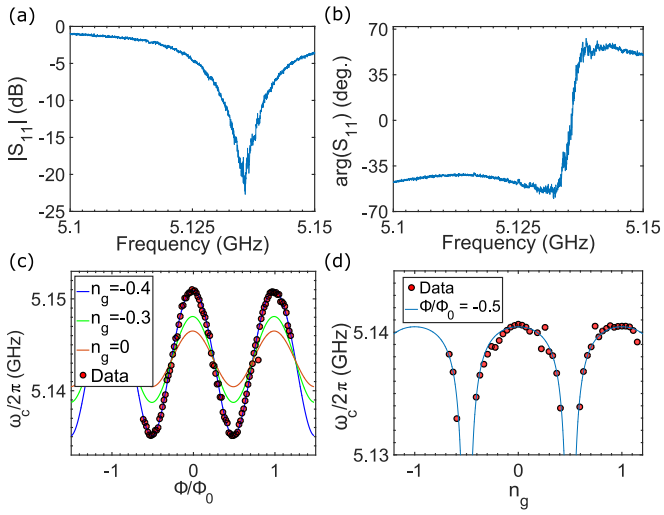

Figure 5. Response of the charge-sensitive microwave cavity, device 1. (a) Magnitude and (b) phase of the microwave reflection. (c) and (d) Represent the frequency shift of the cavity resonance due to magnetic flux Φ in the superconducting loop, and the gate charge n_g, respectively. The dots depict the data when the device is biased with (c) $n_g \approx 0.4$ and (d) $\Phi/\Phi_0 \approx 0.5$. The solid curves correspond to the theoretical model assuming the parameters average $E_J = 0.12$ K, $E_J/E_C = 0.45$, junction resistance asymmetry $d = 0.25$, $L = 2.94$ nH, and $C = 325.5$ fF.

4. Experimental results

In the experiments, we use devices made according to the layout shown in figures 3(a) and (b) (bottom row). They are fabricated by shadow mask evaporation of 30 and 60 nm of aluminum, and oxidizing the first layer in order to create the Josephson junctions. We investigate two devices, labeled 1 and 2. The devices are otherwise nominally similar, but differ in the size of the island as displayed in table 1. In the following, unless noted otherwise, we discuss device 1. We also label image panels according to the device in question.

4.1. Basic characterization

The measurements were carried out in a dilution refrigerator with a base temperature of 30 mK. The microwave tones are applied to the port A of figure 3(a), and we record the scattered signal from the same port. Regarding basic characterization, both devices showed very similar behavior. The cavity linewidth below 200 mK was $\kappa/2\pi \approx 7$ MHz. In figures 5(a) and (b) we show examples of the cavity resonance absorption and phase shift. The cavity frequency is sensitive both to flux and charge as seen in figures 5(c) and (d), respectively. The solid lines represent a theoretical fit produced by numerical diagonalization of the coupled qubit–resonator Hamiltonian, displaying an excellent agreement.

Around the gate bias points $n_g = 1/2$, where the maximum $\frac{\partial \omega_c}{\partial n_g}$ takes place, the cavity resonance becomes smeared out due to enhanced decay or dephasing due to background charge fluctuations. The maximum radiation–pressure couplings, expected to appear in this region by figures 4(a) and (b) in the charge qubit limit, are hence not available. We thus have selected to operate at $n_g \simeq 0.4$ where the cavity resonance is stable, although somewhat broadened compared to the value at $n_g \simeq 0.0$.

We now turn the discussion on observing the quartz vibrations by cavity optomechanical means. We first studied the driven motion by exciting the quartz through the actuation pad (labeled H in figure 3(a)), and probed possible nonlinear changes under an intense driving. A piezo charge which is a substantial fraction of one electron will change the time averaged cavity response (see figure 5(d)), causing a clear signature in the S_{11} response to a weak probe tone. Figure 6 shows this type of the detection, revealing the lowest shear mode resonance at the expected frequency. From the simulations, we obtain an independent estimate of the driven piezo charge $\sim 0.1\ e$, which is in the correct range.

4.2. Detection of piezo thermal motion

The benchmark of cavity optomechanics is the measurement of the motional sidebands due to thermally excited vibrations. Here, a pump tone ω_p is applied near the cavity resonance, and the sidebands appear in the spectrum at the frequencies $\omega_p \pm \omega_m$. The spectral density $S_{out}(\omega)$ in units of quanta (power/bandwidth) divided by system gain $\mathcal{G}$, when the pump is applied at the red or blue sideband, is

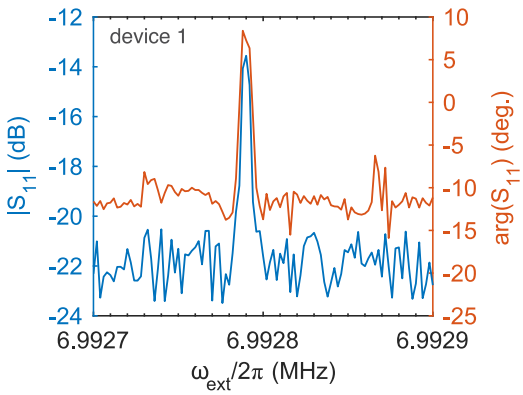

Figure 6. Driven response of the quartz oscillator. The reflection S_{11} of a weak probe tone of a fixed frequency $\sim\omega_c$, while the mechanical vibrations are excited with a voltage of 1 μV at a varying frequency ω_{ext}.

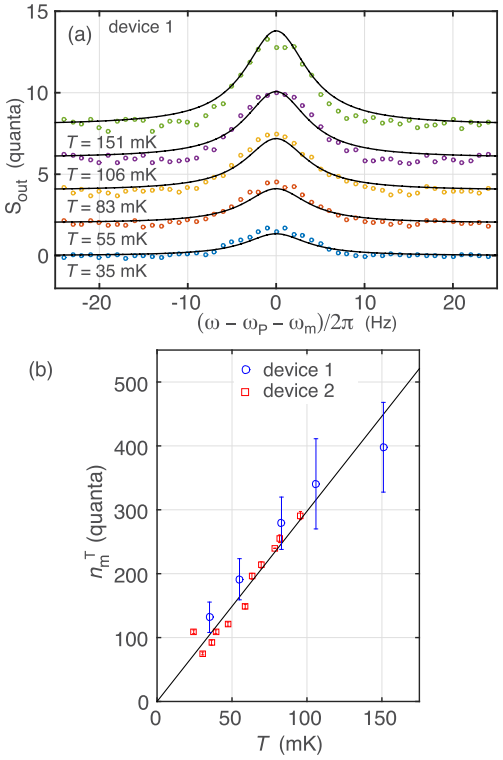

Figure 7. Thermal motion near the quantum limit. (a) Spectral density showing the motional sideband at different cryostat temperatures. The circles are the experimental data, and the solid lines represent the theoretical model, equation (2). The pump frequency was $\omega_p \simeq \omega_c + \omega_m$. The curves are shifted vertically by 2 units for clarity. (b) Phonon number as a function of the cryostat temperature. The dots depict the area below Lorentzian fits to the data, and the solid line represents a linear fit crossing the origin.

$$\frac{S_{\rm out}}{\mathcal{G}} = \frac{\kappa_E}{\kappa}\frac{\gamma\gamma_{\rm opt}}{(\omega \pm \omega_{\rm m})^2 + \gamma_{\rm eff}^2/4} n_{\rm m}^T, \tag{2}$$

which is a Lorentzian centered at the mechanical frequency with respect to the pump frequency.

Our cavities reach a maximum $n_P \lesssim$ 10–20 limited by the Josephson nonlinearity [27, 38]. In figure 7(a) we show the results of such measurement for different cryostat temperatures. The pump power is optimized for maximizing the signal. We use equation (2) to plot the theory curves in figure 7(a). As adjustable parameters, we use $\mathcal{G}$ which is common to all curves, and the conversion factor A from the generator power setting P_0 to the effective coupling, viz. $G = AP_0$. We note that this way we in principle cannot separate the contributions from g_0 and n_P to G, however, we know that cavity nonlinearity limits $n_P \sim$ 10–20, giving a calibration point. The range of estimated n_P here is large because we do not know exactly what amount of nonlinearity corresponds to the maximum signal. We fit $\mathcal{G}$ such that the intermediate-temperature data point (106 mK) in figure 7(a) is fitted properly. This leads to the fact that at lower temperatures, the data points fall above the fit curve. This is visible

also by the fact that the blue points indicate slightly imperfect thermalization. The value of $\mathcal{G}$ is benchmarked against a roughly known fixed point given by the effective noise temperature of the system, setting the noise floor in the spectrum. Here we obtain a reasonable value of ~5 K for the noise temperature. For device 1, we extracted mechanical Q-value of 6.4e5, $g_0/2\pi = 140 \pm 30$ Hz with a maximum $n_\mathrm{P} \approx 15$, reasonably agreeing with the simulated g_0 for our charge focusing design for device 1 when $n_\mathrm{g} \simeq 0.4$ as in the measurement.

The area under the power spectrum in equation (2) is expected to be proportional to the mode temperature, which behavior is qualitatively seen in figure 7(a). To get the points in figure 7(b), we fit a Lorentzian (not limited to equation (2)) to each curve individually. We follow the usual practice and calibrate the equilibrium phonon number n_m^T by relying on $n_\mathrm{m}^T \approx k_B T/\hbar\omega_\mathrm{m}$. Based on the data and a linear fit shown in figure 7(b) for both devices 1 and 2, we conclude that the shear mode thermalizes down to roughly $T \approx 30$ mK, which corresponds to only $n_\mathrm{m}^T = 90 \pm 15$ phonons in the mm-sized vibrating disk.

5. Experimental prospects

In this section we discuss the possibilities to further enhance the coupling or cooperativity in piezo optomechanics in order to control the mechanics via cavity back action. We first review the prospects to increase the coupling in standard microwave optomechanics with linear cavities, where one goal is to approach the single-photon strong coupling condition $g_0 \simeq \kappa$.

5.1. Parametric coupling

Let us now study a mechanical oscillator which directly couples to the cavity frequency. This is the parametric coupling usually encountered in cavity optomechanics. In the following we discuss drumhead or membrane oscillators used in many microwave-frequency experiments [6, 19–22, 24, 39]. Typical parameters for drum oscillator experiments are $\omega_\mathrm{m}/2\pi \approx 10$ MHz, $\kappa/2\pi \approx 500$ kHz, $\gamma/2\pi \approx 100$ Hz. For state-of-the art experiments such as squeezing [20–22], values of cooperativity in the range $C \sim 10^3$–10^4, and decoherence parameter $\eta \sim 10$–10^2 have been reached.

In the microwave regime, the motion changes the capacitance of a microwave cavity having the capacitance C. The total capacitance is the sum of C and a small x-dependent part $C_\mathrm{g}(x)$. The strength of the coupling becomes

$$g_0 \equiv \frac{\partial\omega_\mathrm{c}}{\partial x}x_\mathrm{zp} = \frac{\omega_\mathrm{c}}{2}\frac{C_\mathrm{g}}{C+C_\mathrm{g}}\frac{x_\mathrm{zp}}{d}. \tag{3}$$

The last form used the plate capacitor model, with the vacuum gap d separating the oscillator from the cavity electrode. In order to maximize the coupling, one clearly benefits from a small vacuum gap. In the small-oscillator limit $C_\mathrm{g} \ll C$, the coupling $g_0 \propto d^{-2}$ is a strong function of the gap, and a linear function of the drum surface area. The current experiments typically have roughly $C \sim C_\mathrm{g}$, and exhibit coupling of the order $g_0/2\pi \sim 100$ Hz.

When trying to increase the coupling by reducing the gap, or when making the oscillator larger, one rather soon is faced with the limit $C_\mathrm{g} \gg C$, leading to the fact that the coupling at a fixed cavity frequency does not benefit from increasing the membrane area, but depends only on the vacuum gap inversely. Let us consider a membrane size of 200 μm, with $d = 100$ nm. The membrane metallization will roughly be optimized to cover only the center region of 50 μm. With this values, we obtain $g_0/2\pi \approx 50$ Hz that is lower than state-of-the art. Hence it looks unlikely that the coupling could be much increased in the drum or membrane approach.

5.2. Qubit-mediated effective parametric coupling

In the following we discuss some promising applications for quartz optomechanics, and compare the typical performance indicators obtainable to the state-of-the-art in microwave optomechanics evaluated above in section 5.1. For the current device 2, we obtain $C \sim 0.3$, and decoherence parameter $\eta \sim 10^{-3}$ which clearly are far from those needed for quantum limited work. The corresponding values at the single-quantum level (with $n_\mathrm{P} = 1$), however, are already the same as the drum oscillators exhibit.

As discussed in section 3, the optimal island size for maximizing g_0 is a balance between the piezo charge sensed by the qubit, and increased qubit capacitance which reduces the charge dispersion. Device 3 (see table 1) with a very large ~$(380\ \mu\mathrm{m})^2$ sized island is expected to be relatively close to an optimum, yielding $g_0/2\pi \sim 18$ kHz. In stark contrast to true parametrical coupling, the qubit–mediated coupling thus scales very favorably in the large-size limit. The large size, indeed, is what cavity optomechanics usually is striving for in the quantum-regime investigations. Besides, large size usually implies enhanced mechanical Q values.

In order to spell out numbers for prospective experiments with optimized devices, we note that now we are limited to about $n_\mathrm{P} = 10$ because of cavity nonlinearity. Device 3 in the current setup would be sideband cooled down to the ground state, $n_\mathrm{m} \lesssim 1$ quanta with the current mechanical Q. We now introduce a somewhat

optimized but feasible setup consisting of device 3, and $\kappa/2\pi \approx 1$ MHz, $\gamma/2\pi \approx 1$ Hz (mechanical Q-value of $\sim 10^7$). With such a device we reach $C \sim 10^3$ and $\eta \sim 10$ similar to state-of-the-art drum resonators, but now with a drastically smaller energy pumping. The single-quantum values are, on the other hand, around six orders of magnitude higher than state-of-the-art. We remark that it is generally beneficial to reach a given performance at low pumping, because non-idealities such as heating that the pumping likely introduces.

The experiments that are foreseen in the mentioned optimized setup include new investigations on squeezing, entanglement [40], in particular in potential time-resolved investigations [41], all for the case of a tangible object. With the above values we obtain quantum squeezing of ~5 dB, and entanglement Duan quantity ~0.6 below vacuum between two quartz oscillators (the actual realization still being unspecified).

Another intriguing opportunity offered by our approach is the test of possible extensions of quantum mechanics, in particular that of hypothetical collapse models. These show up as a spurious decoherence channel, and can become visible in a cold oscillator with a long ringdown. [42–44]. With the high Q-values $\sim 10^9$ [45, 46], according to [44] we obtain a spontaneous heating in the DP model of the order 1 mK, which is relevant already in the temperatures encountered in the present experiment.

One can also consider coupling of the piezo motion to the qubit-like mode in the microwave circuit. In the limit of high $E_J/E_C \gg 1$ corresponding to the transmon qubit, the qubit–motion coupling energy becomes (see appendix A) $g'_m = \frac{1}{2}\sqrt{\omega_m \omega_{01}}\sqrt{\frac{C_m}{C_\Sigma}}$, where ω_{01} is the qubit frequency. With an island size of the order $\sim(1\ \text{mm})^2$ one obtains $C_0 \approx 100$ fF, $C_m \approx 1$ fF, and $g'_m/2\pi \approx 5$ MHz, a value similar to micron-sized oscillators, offering prospects to delicate quantum control via the qubit [9, 35, 36, 47, 48].

6. Conclusions

To conclude, monolithic quartz oscillators are a promising platform for physical experiments. They can show exceedingly high quality factors at tens of MHz frequencies, and they present a tangible object in contrast to many other important types of mechanical oscillators. However, creating an intrinsically nonlinear coupling, needed for quantum experiments, from the quartz mechanical vibrations to electrical systems is difficult. In this work, we solve the challenge, and demonstrate cavity optomechanics on such quartz oscillator near the quantum ground state. Focusing of piezo charge allowed coupling of the mechanical oscillations of a mm-sized quartz disk, via a charge qubit, to a microwave cavity. We obtained single-photon coupling energies similar or larger than in state-of-the-art microwave optomechanical setups. As the best future prospect we foresee a design involving a qubit with nearly a mm-size island, allowing for further increasing the coupling by two orders of magnitude. The approach is suitable for such experiments in cavity optomechanics which do not require strong-coupling conditions, but which benefit from a sizable single-phonon coupling and low pumping powers, and long ringdown times. These include macroscopic squeezing and entanglement, as well as tests of extensions of quantum mechanics in unequivocally macroscopic moving bodies.

Acknowledgments

We thank Francesco Massel for useful discussions. This work was supported by the Academy of Finland (contract 250280, CoE LTQ, 275245), the European Research Council (615755-CAVITYQPD), the Horizon 2020 programme (FETPROACT-2016 732894-HOT), the Centre for Quantum Engineering at Aalto University, and by the Finnish Cultural Foundation (Central Fund 00160903). The work benefited from the facilities at the OtaNano—Micronova Nanofabrication Center and at the Low Temperature Laboratory.

Appendix A. Qubit–mechanics interaction

We analyze the Cooper-pair box circuit depicted in figure 8. Although in the real device there are two junctions, the circuit can be represented as a single-junction circuit with a Josephson energy $E_J^* = E_J \cos(\pi\Phi/\Phi_0)$ which depends on the flux bias. The junction capacitance is C_J, the (small) gate capacitance is C_g, and the island self-capacitance is C_0. The total island capacitance is $C_\Sigma = C_J + C_g + C_0$. The dynamical variables are the node flux Θ that corresponds to the qubit degree of freedom, and Θ_m which is that of the mechanical mode.

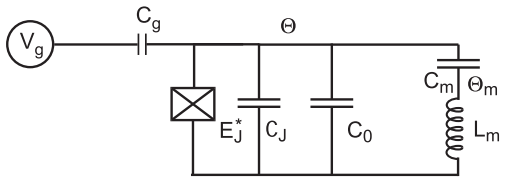

Figure 8. Equivalent circuit of a Cooper-pair box qubit fabricated on top of a piezoelectric substrate. The mechanical mode is modeled as a series resonator with L_m, C_m.

The Lagrangian of the circuit in figure 8 is

$$\mathcal{L} = \frac{1}{2}C_\Sigma\dot{\Theta}^2 + \frac{1}{2}C_g(V_g - \dot{\Theta})^2 - C_g V_g(V_g - \dot{\Theta}) + \frac{1}{2}C_m(\dot{\Theta} - \dot{\Theta}_m)^2 + \frac{\Phi_m^2}{2L_m} + E_J^*. \tag{A1}$$

This gives the generalized momenta:

$$p_m = \frac{\partial\mathcal{L}}{\partial\dot{\Theta}_m} = C_m(\dot{\Phi}_m - \dot{\Theta}), \tag{A2}$$

$$p_q = \frac{\partial\mathcal{L}}{\partial\dot{\Theta}} = (C_\Sigma + C_m)\dot{\Phi}_2 - C_m\dot{\Phi}_m. \tag{A3}$$

The corresponding Hamiltonian $H = p_q\dot{\Theta} + p_m\dot{\Theta}_m - \mathcal{L}$ describes the coupled qubit and mechanical modes with the coupling term

$$H_{qm} = \frac{p_q p_m}{C_\Sigma}. \tag{A4}$$

In the charge qubit limit, we express p_q in the basis of charge states of the island. The island charge Q is the sum of the charges on all capacitors connected to the island, and is related to the momenta as follows:

$$Q = \dot{\Theta}(C_J + C_0) + C_m(\dot{\Theta} - \dot{\Theta}_m) + C_g(\dot{\Theta} - V_g) = p_q - C_g V_g. \tag{A5}$$

Restricting to the two lowest charge states spanning the two qubit states, we have $Q = -e\sigma_z$. Thus equation (A4) becomes

$$H_{qm} = \frac{(Q + C_g V_g)p_m}{C_\Sigma} = \frac{2E_C}{e}\sqrt{\frac{C_m\hbar\omega_m}{2}}\, i\sigma_z(b^\dagger - b) \equiv g_m i\sigma_z(b^\dagger - b). \tag{A6}$$

In the high-capacitance limit relevant for the transmon qubit or phase qubit, one expresses the qubit momentum p_q in the harmonic oscillator basis:

$$Q = \sqrt{\frac{C_\Sigma\hbar\omega_0}{2}}\,\sigma_x, \tag{A7}$$

where $\omega_0 = 1/\sqrt{L_J C_\Sigma}$ is the frequency of small oscillations of the qubit mode. We get the transmon–mechanics coupling

$$H'_{qm} = \frac{\hbar}{2C_\Sigma}\sqrt{\omega_m\omega_0 C_m C_\Sigma}\; i\sigma_x(b^\dagger - b) \equiv g'_m i\sigma_x(b^\dagger - b). \tag{A8}$$

References

[1] Nakamura Y, Pashkin Y A and Tsai J 1999 *Nature* **398** 786
[2] Vion D, Aassime A, Cottet A, Joyez P, Pothier H, Urbina C, Esteve D and Devoret M H 2002 *Science* **296** 886
[3] Hofheinz M *et al* 2009 *Nature* **459** 546
[4] Vlastakis B, Kirchmair G, Leghtas Z, Nigg S E, Frunzio L, Girvin S M, Mirrahimi M, Devoret M H and Schoelkopf R J 2013 *Science* **342** 607
[5] O'Connell A D *et al* 2010 *Nature* **464** 697
[6] Teufel J, Donner T, Li D, Harlow J, Allman M, Cicak K, Sirois A, Whittaker J D, Lehnert K and Simmonds R W 2011 *Nature* **475** 359
[7] Chan J, Alegre T M, Safavi-Naeini A H, Hill J T, Krause A, Gröblacher S, Aspelmeyer M and Painter O 2011 *Nature* **478** 89
[8] LaHaye M, Buu O, Camarota B and Schwab K 2004 *Science* **304** 74

[9] Etaki S, Poot M, Mahboob I, Onomitsu K, Yamaguchi H and Van der Zant H 2008 *Nat. Phys.* **4** 785
[10] Anetsberger G, Arcizet O, Unterreithmeier Q P, Rivière R, Schliesser A, Weig E M, Kotthaus J P and Kippenberg T J 2009 *Nat. Phys.* **5** 909
[11] Aspelmeyer M, Kippenberg T J and Marquardt F 2014 *Rev. Mod. Phys.* **86** 1391
[12] Arcizet O, Cohadon P-F, Briant T, Pinard M and Heidmann A 2006 *Nature* **444** 71
[13] Gigan S, Böhm H, Paternostro M, Blaser F, Langer G, Hertzberg J, Schwab K, Bäuerle D, Aspelmeyer M and Zeilinger A 2006 *Nature* **444** 67
[14] Gröblacher S, Hertzberg J B, Vanner M R, Cole G D, Gigan S, Schwab K and Aspelmeyer M 2009 *Nat. Phys.* **5** 485
[15] Metzger C H and Karrai K 2004 *Nature* **432** 1002
[16] Kleckner D and Bouwmeester D 2006 *Nature* **444** 75
[17] Vinante A, Bahrami M, Bassi A, Usenko O, Wijts G and Oosterkamp T 2016 *Phys. Rev. Lett.* **116** 090402
[18] Sankey J C, Yang C, Zwickl B M, Jayich A M and Harris J G 2010 *Nat. Phys.* **6** 707
[19] Palomaki T, Teufel J, Simmonds R and Lehnert K 2013 *Science* **342** 710
[20] Wollman E E, Lei C, Weinstein A, Suh J, Kronwald A, Marquardt F, Clerk A and Schwab K 2015 *Science* **349** 952
[21] Pirkkalainen J-M, Damskägg E, Brandt M, Massel F and Sillanpää M 2015 *Phys. Rev. Lett.* **115** 243601
[22] Lecocq F, Clark J B, Simmonds R W, Aumentado J and Teufel J D 2015 *Phys. Rev. Lett.* X **5** 041037
[23] Abbott B *et al* 2009 *New J. Phys.* **11** 073032
[24] Yuan M, Singh V, Blanter Y M and Steele G A 2015 *Nat. Commun.* **6** 8491
[25] Heikkilä T T, Massel F, Tuorila J, Khan R and Sillanpää M A 2014 *Phys. Rev. Lett.* **112** 203603
[26] Rimberg A J, Blencowe M P, Armour A D and Nation P D 2014 *New J. Phys.* **16** 055008
[27] Pirkkalainen J-M, Cho S, Massel F, Tuorila J, Heikkilä T, Hakonen P and Sillanpää M 2015 *Nat. Commun.* **6** 6981
[28] Shevchuk O, Steele G A and Blanter Y M 2017 *Phys. Rev.* B **96** 014508
[29] Woolley M, Emzir M, Milburn G, Jerger M, Goryachev M, Tobar M and Fedorov A 2016 *Phys. Rev.* B **93** 224518
[30] Onoe M 2005 Effect of energy trapping on performance of QCM *Proc. of the 2005 IEEE Int. Frequency Control Symp. and Exposition* (Piscataway, NJ: IEEE) pp 433–41
[31] Dataint J, Zarka A, Capelle B and Epelboin Y 1998 *Proc. of the 1998 IEEE International Frequency Control Symp.* pp 882–90
[32] Hirama K, Aoyama Y and Naito M 1997 *Japan. J. Appl. Phys.* **36** 6432
[33] Cumpson P and Seah M 1990 *Meas. Sci. Technol.* **1** 544
[34] Via G, Kirchmair G and Romero-Isart O 2015 *Phys. Rev. Lett.* **114** 143602
[35] LaHaye M, Suh J, Echternach P, Schwab K C and Roukes M L 2009 *Nature* **459** 960
[36] Pirkkalainen J-M, Cho S, Li J, Paraoanu G, Hakonen P and Sillanpää M 2013 *Nature* **494** 211
[37] Niemczyk T *et al* 2010 *Nat. Phys.* **6** 772
[38] Sillanpää M A, Roschier L and Hakonen P J 2004 *Phys. Rev. Lett.* **93** 066805
[39] Noguchi A, Yamazaki R, Ataka M, Fujita H, Tabuchi Y, Ishikawa T, Usami K and Nakamura Y 2016 *New J. Phys.* **18** 103036
[40] Woolley M J and Clerk A A 2014 *Phys. Rev.* A **89** 063805
[41] Martin J and Vennin V 2016 *Phys. Rev.* A **94** 052135
[42] Bahrami M, Paternostro M, Bassi A and Ulbricht H 2014 *Phys. Rev. Lett.* **112** 210404
[43] Nimmrichter S, Hornberger K and Hammerer K 2014 *Phys. Rev. Lett.* **113** 020405
[44] Diósi L 2015 *Phys. Rev. Lett.* **114** 050403
[45] Besson R J 1977 *31st Annual Symp. on Frequency Control* pp 147–52
[46] Goryachev M, Creedon D L, Ivanov E N, Galliou S, Bourquin R and Tobar M E 2012 *Appl. Phys. Lett.* **100** 243504
[47] Gustafsson M V, Aref T, Kockum A F, Ekström M K, Johansson G and Delsing P 2014 *Science* **346** 207
[48] Lecocq F, Teufel J D, Aumentado J and Simmonds R W 2015 *Nat. Phys.* **11** 635